Volume 4 | Number 6 | November 2017 | Pages 935–1202

Materials Horizons

rsc.li/materials-horizons

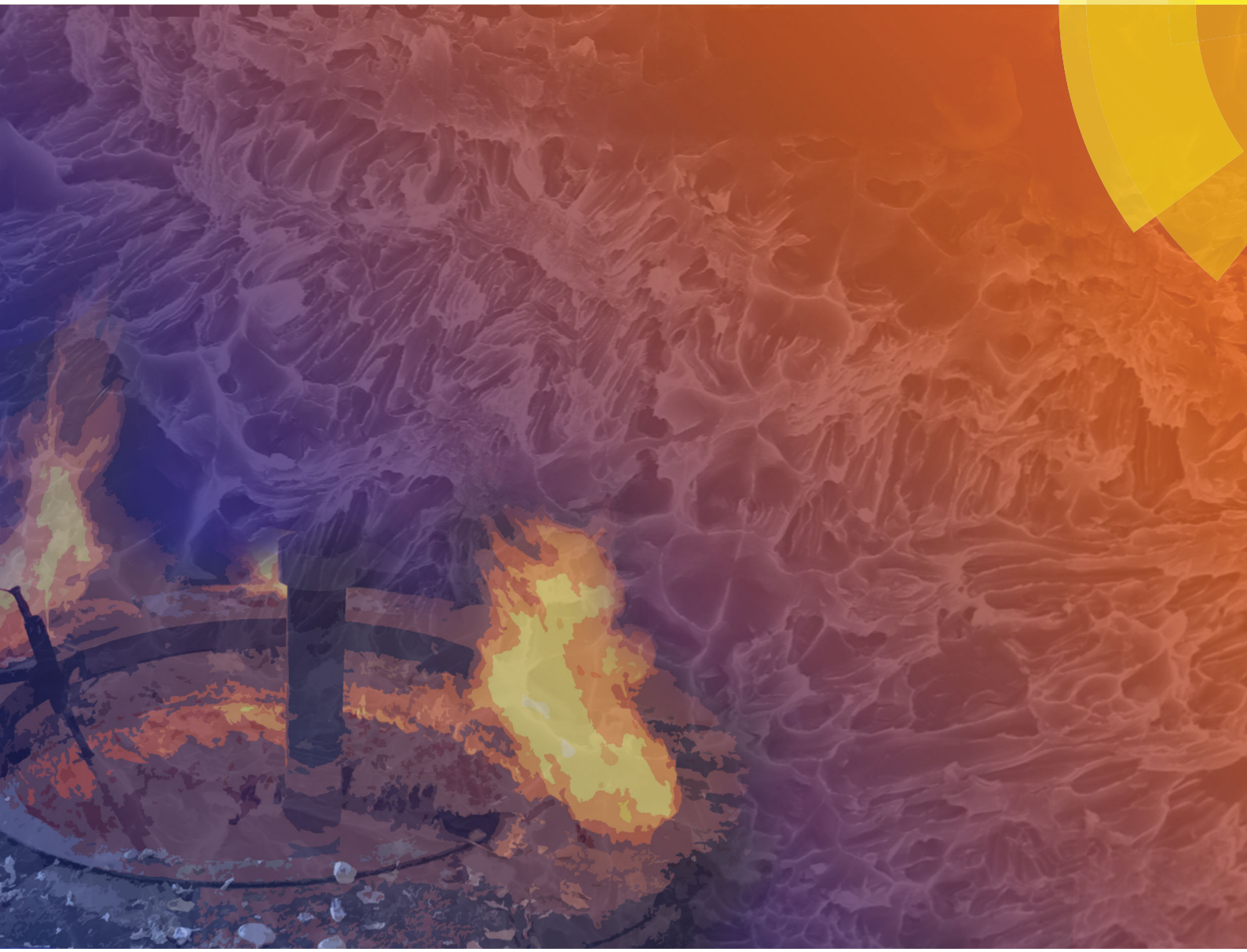

ISSN 2051-6347

ROYAL SOCIETY OF CHEMISTRY

COMMUNICATION

Orlando R. Rios, Scott K. McCall *et al.*

High performance aluminum–cerium alloys for high-temperature applications

Materials Horizons

COMMUNICATION

Cite this: *Mater. Horiz.*, 2017, **4**, 1070

Received 2nd June 2017,
Accepted 25th July 2017

DOI: 10.1039/c7mh00391a

rsc.li/materials-horizons

High performance aluminum–cerium alloys for high-temperature applications†

Zachary C. Sims,[a] Orlando R. Rios,*[a] David Weiss,[b] Patrice E. A. Turchi,[c] Aurelien Perron,[c] Jonathan R. I. Lee,[c] Tian T. Li,[c] Joshua A. Hammons,[c] Michael Bagge-Hansen,[c] Trevor M. Willey,[c] Ke An,[a] Yan Chen,[a] Alex H. King[d] and Scott K. McCall*[c]

Light-weight high-temperature alloys are important to the transportation industry where weight, cost, and operating temperature are major factors in the design of energy efficient vehicles. Aluminum alloys fill this gap economically but lack high-temperature mechanical performance. Alloying aluminum with cerium creates a highly castable alloy, compatible with traditional aluminum alloy additions, that exhibits dramatically improved high-temperature performance. These compositions display a room temperature ultimate tensile strength of 400 MPa and yield strength of 320 MPa, with 80% mechanical property retention at 240 °C. A mechanism is identified that addresses the mechanical property stability of the Al-alloys to at least 300 °C and their microstructural stability to above 500 °C which may enable applications without the need for heat treatment. Finally, neutron diffraction under load provides insight into the unusual mechanisms driving the mechanical strength.

Conceptual insights

The plethora of industrial by-products is a pervasive issue plaguing manufacturing. This report exemplifies how low value materials may be repurposed to develop high performance products with exceptional value, a methodology with broad ramifications. We introduce a remarkable new class of lightweight alloys cast from aluminum and cerium, an abundant by-product of rare-earth mining. The strong reaction affinity between the lanthanide, aluminum, and alloying elements provide large chemical driving forces that activate potent strengthening mechanisms which remain thermodynamically stable at elevated temperatures. Reactive alloy chemistries are commonly used in catalysis, however their use in alloy development is underexplored. We discuss an approach to alloy development that hinges on the direct solidification of reactive phases into thermodynamically stable nanoscale architectures. Unlike other aluminum alloys, whose mechanical properties rely on solid state precipitation of metastable intermetallics or local compositional modulations produced during heat treatment; mechanical properties are tailored during casting through compositional modifications. In most cases, heat treatment, post-heat-treatment machining and associated cost and production rate limitations are eliminated. The thermodynamic mechanisms are analyzed using computational thermodynamics and are broadly applicable to other alloy systems such as Fe, Mg, Ti, and Cu that currently rely on thermomechanical processing to disperse metastable strengthening phases.

Aluminum alloys are desirable as structural materials due to their outstanding castability, excellent mechanical properties, and low cost. They occupy the gap between inexpensive but dense iron alloys and costly, high-performance titanium alloys. Within the transportation sector, the high strength to weight ratio, corrosion resistance, and high thermal conductivity of aluminum alloys have long been important for the automotive and aerospace industries and demand continues to expand due to the promise of improved performance and fuel economy. This paper describes a new family of economically competitive aluminum alloys containing 6–16 weight per cent (wt%) cerium which exhibits dramatically improved high-temperature mechanical properties, in addition to improved castability and thermal stability when compared to existing aluminum alloys. Furthermore, the Al–Ce alloys may not require post-casting heat treatment, which adds significantly to the manufacturing cost in terms of energy, time, and infrastructure requirements.

Castable engineering alloys are typically strengthened through precipitation of intermetallic phases from alloying elements dissolved during the casting process or driven into solution by heat-treating.[1,2] These strengthening precipitates improve alloy performance by increasing stiffness and strength, while lowering thermal expansion;[3,4] however they reside in kinetically frozen high energy architectures along chemical potential gradients that lead to instabilities at elevated temperatures.[5] The high mobility of traditional alloying elements leads to coarsening through processes such as Ostwald ripening; thus, prolonged exposure to high temperatures leads to dramatic changes in the microstructure and a corresponding degradation

[a] *Oak Ridge National Laboratory, 1 Bethel Valley Rd, Oak Ridge, TN, 37831, USA. E-mail: rioso@ornl.gov*
[b] *Eck Industries, 1602 N 8th St, Manitowoc, WI 54220, USA*
[c] *Lawrence Livermore National Laboratory, 7000 East Ave, Livermore, CA 94550, USA. E-mail: mccall10@llnl.gov*
[d] *Ames Laboratory, 311 Iowa State University, Ames, IA 50011, USA*
† Electronic supplementary information (ESI) available. See DOI: 10.1039/c7mh00391a

of mechanical properties. The loss of mechanical performance binds the maximum operating temperature near the alloy aging temperature during the final step of heat treatment (155–190 °C for most Al alloys). This limitation becomes particularly significant for internal combustion engines, which benefit from lightweight materials compatible with higher temperatures for both the engine and nearby components.

Research developing aluminum alloys with improved high temperature performance has principally focused on systems such as Al–Sc, Al–Zr, and Al–V which form stable L_{12} precipitates. The alloy strengthening Al_3X (X = Sc, Zr, V) precipitates are stabilized on the basis of lattice coherence with the fcc aluminum, creating interfacial strain which increases thermodynamic stability and acts as a creep-diffusion barrier. This coherence breaks down above the conversion temperature, *e.g.* about 300 °C for Al–Sc,[6] resulting in the loss of high-temperature performance.

In contrast, Al–Ce based alloys remain thermodynamically stable, independent of their mode of preparation (*e.g.* extruded, wrought, cast). For example, thermo-mechanical processing *via* extrusion of the binary alloy results in 400 MPa ultimate tensile strength (UTS) and 340 MPa yield strength, while hot isostatic pressing (HIP), equivalent to fully dense casting, leads to 280 MPa UTS and 220 MPa yield. The mechanical properties of Al–Ce alloys using an extrusion ratio of 3 : 1 are competitive with leading high temperature wrought alloys such as A2618 (440 MPa UTS) and A4032 (380 MPa UTS) which typically require extrusion ratios exceeding 10 : 1. The applications space for wrought materials is limited by the energy intensive processing associated with producing engineered metastable structures. In contrast, highly castable Al–Ce alloys form structures in thermodynamic equilibrium and remain so until near their melting point. This study focuses on alloys formed by casting rather than alternative processing methods due to the application versatility arising from their ability to adopt a greater range and complexity of structures. Characterization and correlation of the composition, microstructure, and mechanical behavior of cast Al–Ce-based alloys was conducted to understand the origin and mechanisms of their highly desirable performance reported previously at room temperature[7] and, as demonstrated here, at elevated temperatures, with the implicit understanding that thermo-mechanical processing should further enhance the mechanical properties.

These behaviors are driven by the exceptional change in Ce solubility between the liquid and solid phases of aluminum near the eutectic point, which leads to a highly stable intermetallic precipitating into a nano-scale architecture during initial solidification. The superior elongation of cast Al–Ce alloys compared to many commercial Al-alloys is illustrated in Fig. 1a. The intermetallic secondary phases are far more brittle than the surrounding aluminum matrix, and as a result, elongation to failure is driven down as intermetallic content increases.[4,8] The retention of mechanical properties at elevated temperatures is demonstrated in Fig. 1b where the ratio of the 300 °C to room temperature yield strength is compared against the ratio of the 300 °C to room temperature UTS. The Ce alloys retain over 60% of their room-temperature yield and more than 40% of their UTS at 300 °C. This compares favorably to traditional aluminum alloys which at best do not exceed 45% yield and 50% UTS retention values at 300 °C. Incorporation of traditional Al alloying elements such as Si and/or Mg into the Al–Ce parent does not degrade the thermomechanical behavior (Fig. 1b inset) at elevated temperature. Instead, thermodynamic stability, intermetallic morphology, and coherent interfaces (see Fig. S1, ESI†) play a critical role in retention of high temperature mechanical properties.[9] Since these properties are intrinsic to Al–Ce alloys, including ternary and quaternary members, the entire family exhibits significantly greater retention of yield stress at elevated temperatures than traditional Al alloys while maintaining an above average level of UTS (as shown in the blue shaded regions Fig. 1b).

This superior mechanical property retention in the Al–Ce alloys can be understood in terms of the behavior of their constituent phases at elevated temperatures, specifically the solubility and diffusion of Ce. Several atomic percent of common aluminum alloying additions, such as Cu, Si, and Mg can dissolve into the aluminum matrix during a heat treatment as their solubility increases with temperature (see the ESI†).[8] These are the primary additions in the A206, A356, and A535 alloys, respectively. Quenching retains the solute atoms in a supersaturated solution and enables finely dispersed precipitate formation *via* age hardening, which may be accelerated by soaking at 100—200 °C.[10] Nonetheless, this same solubility limits the high-temperature stability of the alloy due to precipitate dissolution and the resulting changes to the microstructure. In contrast to the common Al-alloying elements, the solubility of Ce in solid aluminum is very low. Near the eutectic temperature (642 °C), the upper limit of solubility is less than 0.005 wt% Ce in Al[11] and may be closer to 0.00012 wt% Ce in Al; as compared to Cu, which has a solubility exceeding 5 wt% by 600 °C.[8] Even Sc, which leads to the most competitive high-temperature alloys has a solubility of 0.2 wt% at 600 °C, exceeding the solid solubility of Ce by several orders of magnitude.[12] The Ce values are consistent with the CALPHAD thermodynamic assessment of the Al–Ce binary phase diagram (Fig. 1c and d) which predicts a similarly low solubility for Ce in the Al matrix,[13] and renders the strengthening intermetallic, $Al_{11}Ce_3$, far more stable against dissolution in solid Al than the intermetallics of standard commercial alloys. Dissolution of strengthening phases into the aluminum matrix is illustrated in property diagrams (Fig. 1e) where the fraction of intermetallic precipitates retained decreases with increasing temperature. It is evident that the phase fraction of intermetallic, in this case $Al_{11}Ce_3$, retained at elevated temperatures far exceeds any of the other alloying elements. Electron microscopy data (Fig. 2) reinforce the assignment of near-zero solubility of Ce in Al and intermetallic stability of $Al_{11}Ce_3$ at elevated temperatures. Fig. 2c contains an Energy Dispersive X-ray Spectroscopy (EDS) map of a 10 wt% cerium alloy inset in the high angle annular dark-field transmission electron microscopy (HAADF TEM) image (see the ESI† for additional images). The EDS map reveals a distinct dividing line between the Al rich phase and the Ce rich intermetallic,

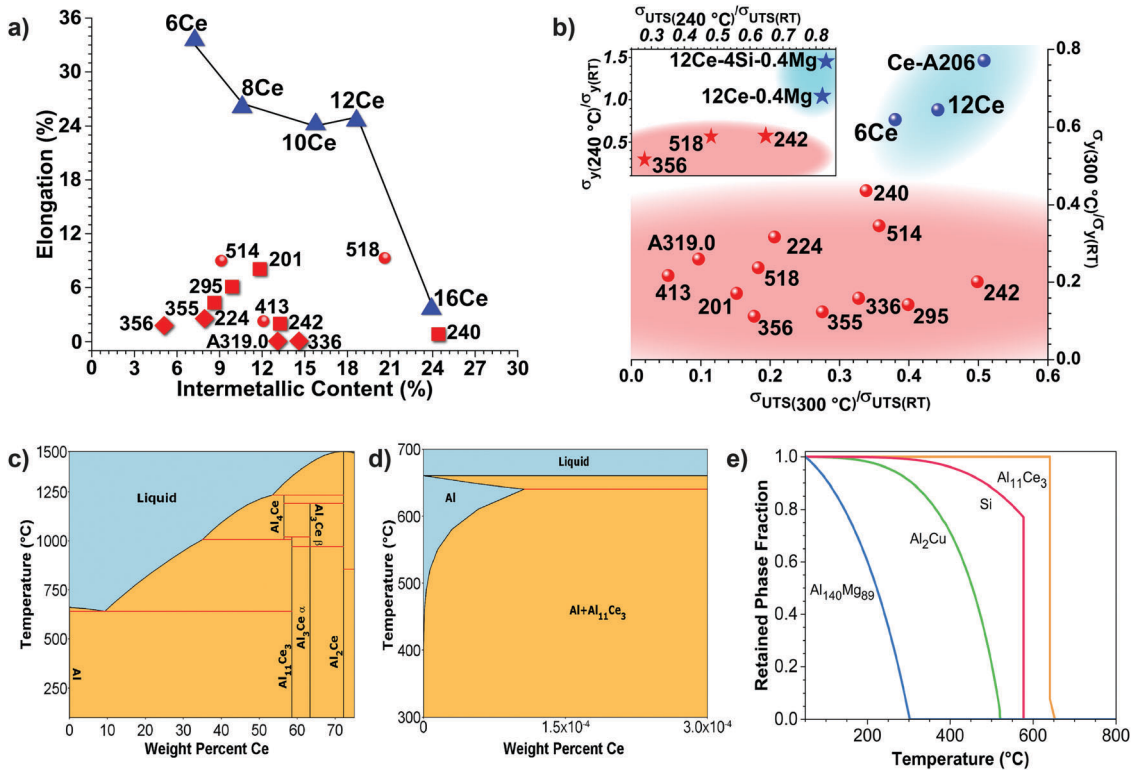

Fig. 1 Al–Ce alloy properties. (a) Elongation *vs.* intermetallic content for Al–Ce (wt%) alloys (blue triangles) with a line to guide the eye compared to traditional aluminum alloys (red). (b) Ratio of 300 °C to room temperature yield strength *vs.* ratio of ultimate tensile strength at 300 °C to room temperature, demonstrating superior thermomechanical stability for Al–Ce alloys compared to standard alloys.[8] Ce–A206 is A206 alloy with 8 wt% Ce. The inset shows Al–Ce based alloys at 240 °C against standard alloys at 200 °C. Al–Ce–Si–Mg alloys show increased yield at elevated temperature and Al–Ce–Mg shows no decrease relative to room temperature. (c and d) An Al-rich region of the Al–Ce phase diagram based on (a) where the Al matrix exhibits almost no Ce solubility. (e) Phase stability of major precipitate phase fraction relative to room temperature in aluminum alloys highlighting the thermal stability of $Al_{11}Ce_3$. Color code: 500 series (blue), 200 series (green), 300 series (red), and the new Al–10Ce (wt%) alloy (orange).

while detailed TEM studies show a coherent phase boundary. The lack of Ce dispersion at the phase boundary reflects the thermodynamic stability of $Al_{11}Ce_3$ (ΔH_f = −42.7 kJ mol^{-1} at room temperature relative to Al and Ce) which drives the Ce toward intermetallic formation.[13]

In addition to their low solubility, the large size of the Ce atoms results in a reduced diffusion coefficient when compared to other alloying elements. As an illustration, the diffusion coefficient for Ce at 500 °C is 5.7 × 10^{-14} cm^2 s^{-1}, which is about 10 000 times smaller than for Cu, 6.0 × 10^{-10} cm^2 s^{-1} or Mg, 1.4 × 10^{-9} cm^2 s^{-1}, at comparable temperatures.[2,14] Strong vacancy binding to Ce atoms[15] further decreases degradation of the $Al_{11}Ce_3$ intermetallics as it impedes and, therefore, reduces vacancy diffusion—the dominant transport mechanism for solute atoms within the matrix.[16]

Experimental evidence supporting the low solubility and diffusion of the Ce within the Al–Ce systems is provided by the scanning electron microscopy (SEM) back-scatter images of the as-cast and heat-treated 12 wt% Ce alloys respectively in Fig. 2(a and b). The as-cast alloys show a very fine interconnected eutectic microstructure (white) and the pure aluminum phase (gray). The scale of the laths, as small as 100 nm, along with their uniform distribution, and interdendritic spacing all aid in improving the alloy mechanical properties.[8,17] Exposing the same alloy to a 20 hour soak at 520 °C results in a eutectic microstructure that has undergone only minor morphological changes. Instead of thin and interconnected laths, they have rounded in many places and become less interconnected. This represents a localized minimization of the microconstituent surface energy at the eutectic through interdiffusion within the intermetallic and accompanying spheroidization, rather than bulk diffusion through the matrix. The overall scale of the intermetallic phase has not changed: laths and rods remain at widths near 100 nm, and the phase fractions are consistent across samples, thereby demonstrating that the conversion temperature is above 520 °C. The fcc phase regions remain relatively small and well distributed throughout the sample after heat-treatment. Thus, a combination of low Ce solubility in the Al matrix and low Ce diffusion coefficients avoids coarsening mechanisms through Ostwald ripening, while the high thermodynamic stability of the $Al_{11}Ce_3$ intermetallic resists substantial microstructural evolution in the Al–Ce alloys and, by extension, degraded mechanical properties.

The fracture surfaces for Al–12Ce and Al–16Ce (wt%) are shown in Fig. 2d and e, respectively. Significant dimpling, a characteristic of ductile fracture, dominates the fracture surface of Al–12Ce (wt%). Primary $Al_{11}Ce_3$ solidification begins around 10 wt% Ce addition, just beyond the Ce–Al eutectic point (Fig. 1c). The cooling rates of the experimental castings

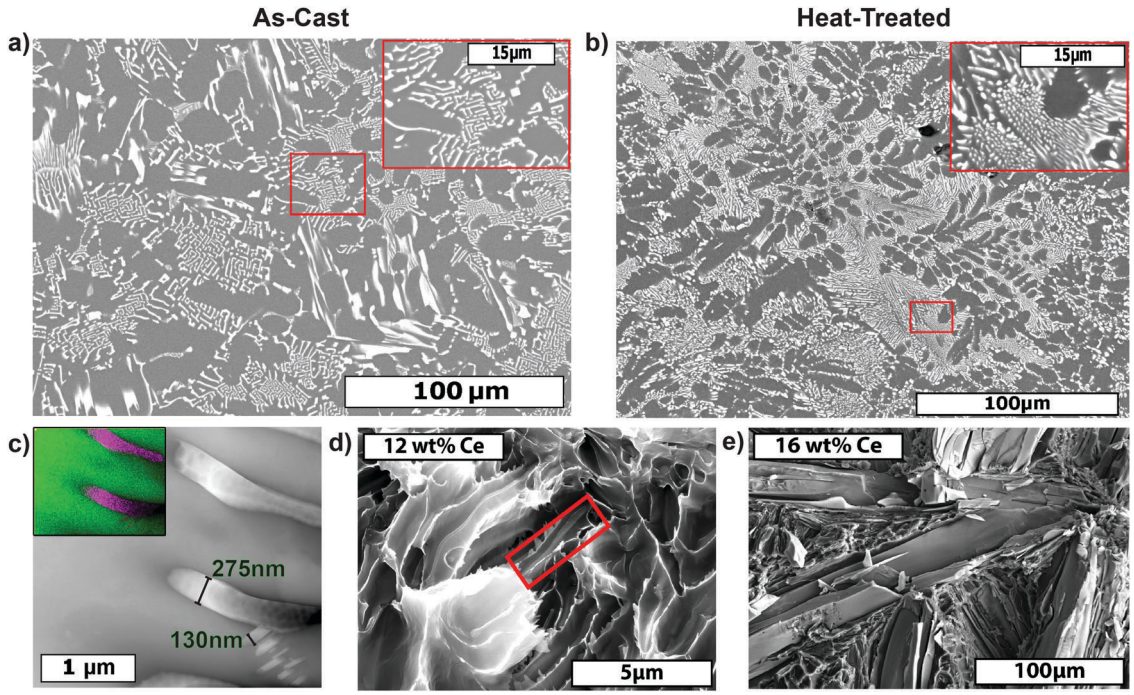

Fig. 2 Micrographs of the Al–12Ce (wt%) alloy (a) as-cast, and (b) after T6 heat treatment showing mild spheroidization but no change in the larger features. (c) TEM HAADF image of Al–10Ce (wt%) where the $Al_{11}Ce_3$ laths are 100–200 nm wide. The false color inset shows the $Al_{11}Ce_3$ regions (purple in the EDS map). (d and e) Fracture surfaces of Al–12Ce and Al–16Ce (wt%), respectively, illustrating ductile fracture in the former and a mix of ductile and brittle fracture in the latter. Red area in (d) shows fracture along a eutectic intermetallic lath with ductile fracture surrounding. Ductile fracture can be observed in the eutectic zone surrounding the brittle primary crystals in (e). These eutectic zones lead to the elevated ductility of this alloy over alloys with a similar intermetallic content. Note the different scale bars between (d and e).

were sufficiently fast to undercool the 12 wt% alloy into the eutectic region, while at 16 wt% Ce, large primary crystals of $Al_{11}Ce_3$ precipitate surrounded by eutectic laths. The large crystals promote brittle fracture, yet some ductility remains due to the surrounding matrix-eutectic ductile fracture mechanism. The dominant brittle fracture along the crystal faces leads to the drastic drop in ductility between the 12 wt% and 16 wt% Ce alloys as shown in Fig. 1a. Even then, ductility values remain comparable to that of many commercial aluminum alloys with an equivalent intermetallic content.

The alloy mechanical properties are significantly improved with small quantities of ternary and quaternary additions. Representative castings of Al–12Ce–4Si (wt%) and Al–12Ce–4Si–0.4Mg (wt%) illustrate these properties. Cerium reacts favorably with many traditional solutionizing elements, including Mg and Si, to form thermally stable intermetallics without microstructural coarsening in the solid state. Small additions of Si lead to the tetragonal intermetallic $Ce(Si_{1-x}Al_x)_2$, with x = 0.1–0.9, identified in Fig. 3a as the τ_1 phase (I_{41}/amd space group) which extends across the central portion of the phase diagram and exhibits a high range of temperature stability in the aluminum matrix once formed,[13,18,19] similar to that of $Al_{11}Ce_3$ in the binary. The low solubility of Ce in Al and Si[20] along with the tight bonding of vacancies to Ce[15] and the formation enthalpy of the τ_1 phase, which reaches a minimum of -67 kJ mol^{-1} near x = 0.5, all contribute to the stability of this phase. The solubility of Si in the Al matrix phase is 1.5 wt% at high temperatures and it is possible to quench a supersaturated solid solution to 11 wt%, whereas the low mobility and reactivity of Ce leads to immediate intermetallic formation. Thus, the structure of the as-cast Al–Ce–Si comprises $Al_{11}Ce_3$ intermetallic laths formed through an invariant reaction in an Al matrix that seed precipitation of Si from the supersaturated solution as the matrix solidifies. After a T6 heat-treatment the morphology persists, with the precipitates serving as templates for the ternary $Ce(Si_{1-x}Al_x)_2$. The associated mechanical properties improve from a yield and UTS of 83 MPa and 150 MPa, respectively to 128 MPa and 255 MPa after a T6 heat treatment. Similarly, the elongation improves from 2% to 8.5% before fracture.

The stability of these multicomponent phases at elevated temperatures was explored through a series of volume averaged ultra-small and small angle X-ray scattering (USAXS/SAXS) measurements. Analysis of the scattering data provides insight into the size, shape, number density, and size dispersion of structural inhomogeneities (*i.e.* intermetallics in the alloys) and, as such, these methods are ideally suited for investigating the structure and structural evolution of these alloys. A T6 heat treated Al–12Ce–4Si–0.4Mg (wt%) specimen was heated in 100 °C increments between which the sample was cooled to room temperature, with measurements performed at both the elevated and base temperature (Fig. 3b). Should any microstructural changes result, deflections would be observed in the scattering vector. The fact that there is no deviation between individual spectra in successive measurements indicates that there are no changes in the underlying microstructure in either

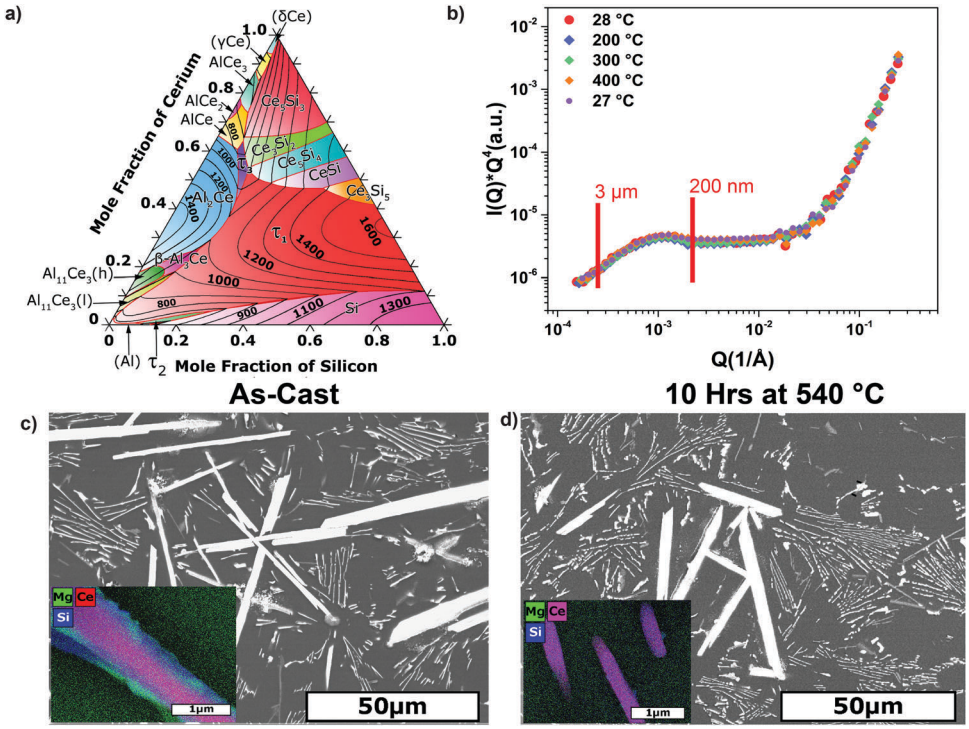

Fig. 3 Thermal stability of the alloy. (a) Al–Ce–Si ternary liquidus projection based on a CALPHAD assessment (see text). (b) USAXS/SAXS for Al–12Ce–4Si–0.4Mg (wt%) illustrating that heating has negligible effect on particle size (or shape: see S3 and S4, ESI†). (c and d) SEM micrograph of Al–12Ce–4Si–0.4Mg (wt%) as-cast and after T6 heat treatment. Insets show EDS of intermetallic precipitates of the same composition (Al contribution removed for clarity) illustrating internal changes in microstructure.

size or shape to at least 400 °C (see the ESI† for a detailed analysis).[21] SEM images before and after heat-treatment of the Al–12Ce–4Si–0.4Mg (wt%) alloy (Fig. 3c and d) further illustrate the high-temperature stability of the system. In the as-cast state, primary crystals of Ce-rich intermetallics are surrounded by thin laths of Al–Si and Al–Si–Mg intermetallics. After 10 h at 540 °C the Mg diffuses uniformly throughout the aluminum matrix while the primary crystals transition to $Ce(Si_{1-x}Al_x)_2$, as illustrated in the TEM false-color images (insets to Fig. 3c and d). The surrounding eutectic displays similar morphological changes to those seen in the binaries with more isolated and less interconnected intermetallic structures forming from surface energy minimization. Thermodynamic stability is important to retain the high temperature mechanical strength, but identification of the underlying strengthening mechanisms requires further investigation.

To this end, neutron diffraction measurements enabled investigation of the mechanical behavior as a function of compressive loading. These experiments focused on the simplest alloys, whose behavior is reflective of this family of materials: the Al–12Ce (wt%) binary and the structurally equivalent Al–12Ce–0.4Mg (wt%) ternary. These specimens provide distinct peaks for both the Al matrix and intermetallic $Al_{11}Ce_3$, as shown in Fig. 4a for the binary alloy. Analysis of these diffraction peaks as a function of loading enables assignment of the lattice strain within each phase, and by extension, identification of load partitioning in the system. Emphasis is placed upon analysis of the diffraction data from the Al matrix because it has a simple cubic unit cell; since the Al–Ce alloys are two component systems, the properties of the complex anisotropic $Al_{11}Ce_3$ intermetallics can then be inferred from the behavior of the Al matrix. Fig. 4b details the true strain behavior of the Al matrix in both the binary and ternary alloys, revealing a three-stage behavior with anomalous lattice strains instead of the linear stress–strain behavior expected in a conventional Al alloy.[22,23] Fig. 4c and d details how the load is partitioned or shared between the two phases present in the alloy. During the initial loading (stage I), the Al matrix and intermetallic deform elastically under low stress (*i.e.* below 50 MPa). After early yielding, there is a transition to stage II, denoted by red arrows in Fig. 4b, where additional stress leads to the Al matrix showing a decelerated lattice strain response while applied stress increases. During this stage, the intermetallic phase carries an increasing share of the applied load. The increasing deformation observed at stage III is triggered (black arrows) once the dislocations reach a critical density and the intermetallic yields. Here, the Al matrix starts to take on more stress, indicated by the increase in slope, and the load partition rebalances between the two phases leading to destructive plastic deformation in the aluminum matrix. The transitive load behavior of Al–Ce and Al–Ce–Mg alloys is similar to the load partitioning characteristics of dispersion strengthened metal matrix composite (MMC) alloys,[24] which exhibit high-strength and good thermal stability.[25] However, Al–Ce alloys differ from MMC alloys in that both the matrix and intermetallic strengthening phase are developed directly from the molten material. This co-precipitation from the melt is significant because

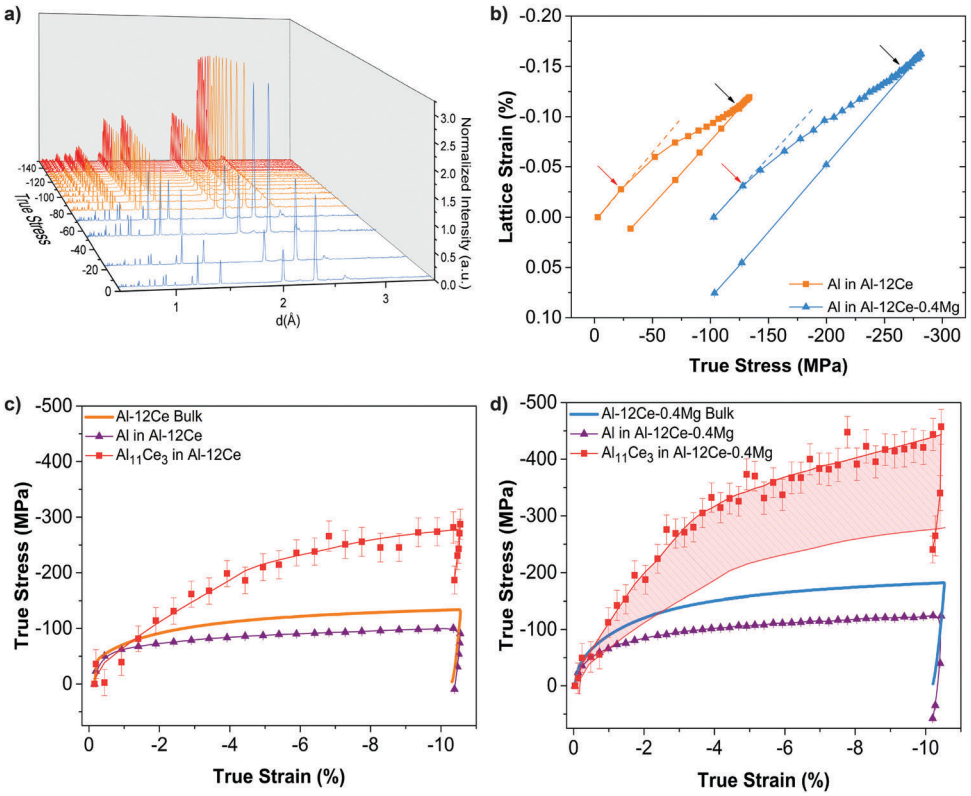

Fig. 4 (a) Neutron spectra showing change in scattering intensity as applied compressive strain increases. (b) Strain measurements of Al–12Ce and Al–12Ce–0.4Mg (wt%) performed under compressive load (the latter is offset by 100 MPa for visibility). Here the arrows denote onset of phases II (red), and III (black) described in the text. (c) Phase load-sharing for Al–12Ce under compressive load. (d) Phase load-sharing for Al–12Ce–0.4 Mg under compressive load. Shaded region denotes difference between binary and ternary alloy composition's mechanical response.

it leads to a distinct load transfer behavior dominated by interfacial micromechanical interaction. The reverse exchange behavior between phase II and III is attributed to elastic saturation in the fine intermetallic phase leading to subsequent plastic flow in the ductile matrix accompanied by cracking in the intermetallic. This cracking leads to isolated nanoparticles with coherent interfaces which strengthen the alloy.

This two-stage complex yield behavior prior to total plastic deformation is a potent mechanism for yield retention at elevated temperature in these alloys. In the initial fully linear elastic region and transitional yield region (*i.e.* 2% offset) the exceptional thermal stability of the Al–Ce intermetallic phase ensures little change to the micro-mechanical interactions between the matrix phase and the strain fields generated by the nearby intermetallic crystals. Furthermore, intermetallic crystals continue to act as powerful sites for dislocation pinning throughout the deformation process. Once plastic deformation begins in the matrix phase, the intermetallic phase takes on proportionally more elastic load. The reduction in yield at high-temperature thus results from the softer aluminum matrix, but the retention occurs through the stable intermetallic phase carrying very similar amounts of elastic strain to room temperature values. At increased temperatures, thermally assisted deformation mechanisms accelerate plastic deformation of the Al matrix phase against the stable intermetallic phase. Increasing the intermetallic content from 7 to 18 wt% increases the UTS retention from 40 to 50%. In the binary alloys, the matrix is devoid of solute, so a minor addition of 0.4 wt% Mg, an efficacious solid solution strengthener in Al, increases the UTS retention from 50 to 80% primarily by strengthening the matrix phase of the base Al–12Ce (wt%) alloy. Thus, the semi-coherency of the interface combined with high-temperature intermetallic phase stability leads the Al–Ce alloys to maintain a high portion of their yield strength at elevated temperatures. By contrast, traditional aluminum alloys, strengthened by metastable phases,[26] tend to breakdown at high-temperature and consequently lead to accelerated weakening of the load carrying capabilities.

A significant residual compressive strain exists in the hard $Al_{11}Ce_3$ phase while a slight tensile load resides in the soft Al matrix, which is expected behavior after unloading given the two-phase coexistence and complex load sharing. Comparing Fig. 4c and d reveals that the strengthening mechanism of the Al–Ce alloy does not change following the addition of Mg. Instead, Mg increases the magnitude of the load which can be carried by the intermetallic phase before dislocation saturation and subsequent redistribution of load to the aluminum matrix. The difference is depicted by the shaded region in Fig. 4d.

The room temperature strength of the Al–Ce alloy family derives from the extremely fine distribution of dendritic intermetallic

phases uniformly across the alloy which forms during casting. The very low solubility of Ce in the solid Al matrix favors retention of this structure to very high temperatures compared to traditional casting Al alloys, and this is reflected in the superior retention of mechanical properties to above 300 °C. These features lead to complex load-sharing in the binary Al–Ce alloy, where slight Mg addition markedly improves the material strength and offers a guide to further improvements in this new class of Al alloys.

In summary, cerium strengthened aluminum alloys exhibit highly desirable behavior for many applications: high ductility, robust room-temperature mechanical properties, exceptional high-temperature mechanical property retention, high tolerance to casting defects, and excellent castability across a broad range of compositions. In fact, the cast materials approach the mechanical properties of traditional wrought alloys. The microstructure remains stable to above 500 °C, corresponding to a homologous temperature (T/T_{Melt}) greater than 0.84, which rivals the stability observed in heat tolerant materials such as superalloys.

Given the high availability and low cost of cerium metal, these alloys are economically viable for large volume industries such as the transportation sector, where their properties make them ideally suited for vehicle lightweighting. Elimination or reduction of heat-treatment amplifies the economic and environmental benefits of lightweighting in the transportation sectors. Adoption of these alloys by industry will not only impact current technologies, but will provide the basis with which to develop the next generation of high temperature aluminum alloys. Finally, by creating demand for Ce, which is overproduced, the economics of rare-earth mining improve.[27] In a typical deposit, one-third to one-half of the rare-earth content by weight is cerium, so converting a by-product into a co-product will help stabilize global production and encourage diversification of the rare-earth supply chain.

Experimental details

CALPHAD thermodynamics

The phase diagrams presented herein have been thermodynamically assessed[13–15,18] within the CALPHAD methodology, and the commercially available software Thermo-Calc has been used to calculate the equilibrium phase diagrams based on a user-defined thermodynamic database.[28] In this approach, the Gibbs energy of individual phases is modeled, and the model parameters are collected in a thermodynamic database. Models for the Gibbs energy are based on the crystal structures of the phases and interaction parameters are assessed to reproduce both the diagrammatic and thermodynamic data available for binary and ternary systems. Phase diagrams of the relevant binaries are included in the ESI.†

Casting and sample characterization

Alloys were cast using industrial practices. Industrial grade ~30 lb aluminum ingots were brought to a molten state in a tilt pour resistive furnace. Once the metal was molten and the temperature stabilized at 750 °C, alloying elements were added one at a time, with cerium being the final addition. If multiple compositions were being cast during a single trial, additional melts were prepared from the heel of the previous melt. The metal was poured into a ceramic lined permanent mold heated to 400 °C; each mold comprised two dog bone style test-bars 25 cm in length. Selections of bars at each composition were heat-treated with either a T6 (10 h at 540 °C, warm water quenched and then artificially aged for 3 h at 150 °C) or T4 heat-treatment (10 h at 540 °C, warm water quenched). The as-cast and heat-treated test-bars were mechanically tested in tension using a United Calibration and Testing Universal Testing machine. For high-temperature measurement test-bar grips were threaded and bars were held at temperature for no less than thirty minutes, after which they were strained under tension until failure.

Gauge lengths of fractured bars were sectioned into 2 mm disks then polished and etched using Keller's reagent. Imaging was performed on a Hitachi S-4700 Cold field emission Scanning Electron Microscope. Phase analysis was completed *via* X-Ray diffraction using the Panalytical X'Pert Pro system combined with Rietveld analysis through the use of the High-Score plus software suite.

TEM measurements

For sample preparation, 3 mm disks were cut from fractured bars and mechanically polished to ~150 μm thickness and then further electro-polished at −15 °C using an 80% methanol/15% perchloric acid/5% HF electrolyte until electron transparent. Measurements were performed using the TitanX Scanning Transmission Electron Microscope at the National Center for Electron Microscopy at the Molecular Foundry located at Lawrence Berkeley National Laboratory. The TitanX was operated at 200 kV for the STEM EDS measurements.

SAXS/USAXS

The USAXS data were collected on a combined Bonse-Hart/Pinhole SAXS/WAXS instrument at 9-IDC at the Advanced Photon Source located at Argonne National Laboratory.[29] All samples were prepared with uniform thicknesses and exposed to a monochromatic 24 keV X-ray beam for two minutes during data collection. With the sample thicknesses known, all USAXS data are calibrated and on an absolute scale.[30] A detailed analysis and additional data are included in the ESI.†

Neutron diffraction under load

The neutron diffraction experiment was conducted at the Vulcan diffractometer[31] at the Spallation Neutron Source (SNS), Oak Ridge National Laboratory. The cylindrical specimen of 10 × 20 mm was mounted horizontally in the loadframe with the axial direction parallel to the loading direction. An extensometer was attached to the specimen for measuring the engineering strain. Compressive loads were applied at a rate of −10 MPa min^{-1} (negative denotes compression) with a 15 min dwell at −25 and −50 MPa in the elastic region. To avoid stress

relaxation during stepwise loading during plastic deformation,[22,32] the specimen was then continuously compressed at a strain rate of $-0.01\ h^{-1}$ until the strain reached -0.1. The specimen was subsequently unloaded at a stress rate of 0.8 MPa min^{-1}. The incident neutron beam, 45° to the loading direction, was focused at the center of the specimen, which remained stationary due to uniform displacement from both sides. The gauge volume was defined to about $5 \times 5 \times 5\ mm^3$ by the incident slits and radial collimators. During the mechanical test, the two detectors, located at −90° and +90° to the incident beam, continuously recorded the diffracted neutrons with the scattering vector parallel to the longitudinal and transverse directions, respectively. The diffraction data were averaged in a 15 min interval using the VDRIVE software. The lattice parameters were extracted from Rietveld refinement of the entire scattering pattern using GSAS and EXPGUI software.

The lattice strain ε of individual phases was calculated by $\varepsilon_x = (L_x - L_{x,0})/L_{x,0}$ along a principal (*i.e.* crystallographic) axis, where the reference $L_{x,0}$ under zero stress was estimated using the result before loading.[33] The corresponding microstress (σ_x) of a phase along the particular axis was obtained by $\sigma_x = E_x \cdot \varepsilon_x$, where E_x is the elastic diffraction constant. E_x was estimated from the linear unloading behaviors which is assumed as an elastic process, by using $E_x = \Delta\sigma_x/\Delta\varepsilon_x$, where $\Delta\sigma_x$ and $\Delta\varepsilon_x$ are the changes of stress and strain, respectively, during the elastic unloading along the particular direction. For the Al matrix phase, the lattice strain and microstress were measured against changes in the fcc lattice parameter "*a*". For an $Al_{11}Ce_3$ intermetallic phase, the behavior along the *b*-axis was selected to represent the behavior of the phase.

Author contributions

D. W., O. R. R., and Z. C. S. produced the samples, P. E. A. T., A. P., O. R. R., and Z. C. S. performed the modeling, J. R. I. L., J. A. H., M. B.-H. and T. M. W. performed the SAXS/USAXS measurements and analysis, T. T. L. provided TEM images and analysis, K. A. and Y. C. performed the neutron measurements, O. R. R. and S. K. M. designed the experimental program and coordinated the project. A. H. K. provided critical insight into the project. All authors contributed to the interpretation of the results. Z. C. S., O. R. R., J. R. I. L., A. P., D. W., and S. K. M. wrote the paper.

Conflicts of interest

There are no conflicts of interest to declare.

Acknowledgements

This research was sponsored by the Critical Materials Institute, an Energy Innovation Hub funded by the U.S. Department of Energy (DOE), Office of Energy Efficiency and Renewable Energy, Advanced Manufacturing Office and Eck Industries. This work was performed under the auspices of the U.S. DOE with ORNL under contract DE-AC05-00OR22725 and with LLNL under Contract DE-AC52-07NA27344. Work at the Molecular Foundry was supported by the Office of Basic Energy Sciences, of the U.S. DOE under Contract No. DE-AC02-05CH11231. The use of the Advanced Photon Source, an Office of Science User Facility operated by Argonne National Laboratory, was supported by the U.S. DOE under Contract No. DE-AC02-06CH11357. The authors thank Dr Jan Ilavsky for support on 9-ID-C of the APS and Dr Melissa Santala for preliminary TEM support.

References

1 S. Otarawanna and A. K. Dahle, *Fundamentals of Aluminium Metallurgy*, Woodhead Publishing, 2011, pp. 141–154, DOI: 10.1533/9780857090256.1.141; R. Lumley, *Fundamentals of Aluminium Metallurgy: Production, Processing and Applications*, Elsevier, London, 2010.
2 L. F. Mondolfo, *Aluminum alloys: Structure and properties*, Butterworths, London, 1976.
3 R. L. Fleischer, *J. Mater. Sci.*, 1987, **22**, 2281–2288; G. H. Garza-Elizondo, A. M. Samuel, S. Valtierra and F. H. Samuel, *Int. J. Metalcast.*, 2017, **11**, 413–427.
4 C. T. Liu, J. Stringer, J. N. Mundy, L. L. Horton and P. Angelini, *Intermetallics*, 1997, **5**, 579–596.
5 S. P. Marsh and M. E. Glicksman, *Acta Mater.*, 1996, **44**, 3761–3771.
6 E. A. Marquis and D. N. Seidman, *Acta Mater.*, 2001, **49**, 1909–1919.
7 Z. C. Sims, D. Weiss, S. K. McCall, M. A. McGuire, R. T. Ott, T. Geer, O. Rios and P. A. E. Turchi, *JOM*, 2016, **68**, 1940–1947.
8 *Aluminum and Aluminum Alloys*, ed. J. R. Davis, ASM International, Materials Park, OH, 1993.
9 V. V. Zakharov, *Met. Sci. Heat Treat.*, 2003, **45**, 246–253; M. E. van Dalen, D. C. Dunand and D. N. Seidman, *Acta Mater.*, 2005, **53**, 4225–4235; M. S. Zedalis and M. E. Fine, *MTA*, 1986, **17**, 2187–2198; K. E. Knipling, D. C. Dunand and D. N. Seidman, *Z. MetaIlkd.*, 2006, **97**, 246–265.
10 H. E. Boyer, *Metallogr., Microstruct., Anal.*, 2013, **2**, 190–195; M. V. Glazoff, V. S. Zolotorevsky and N. A. Belov, *Casting Aluminum Alloys*, Elsevier, New York, 2010.
11 C. Weiping, *J. Mater. Sci. Lett.*, 1997, **16**, 1824–1826; K. A. Gschneidner Jr and F. W. Calderwood, *HPCRE*, Elsevier, 1986, vol. 8, pp. 1–161.
12 M. E. Drits, E. S. Kadaner and N. D. Shoa, *Russ. Metall.*, 1969, **1**, 113.
13 M. C. Gao, N. Ünlü, G. J. Shiflet, M. Mihalkovic and M. Widom, *Metall. Mater. Trans. A*, 2005, **36**, 3269–3279.
14 Y. Du, Y. A. Chang, B. Huang, W. Gong, Z. Jin, H. Xu, Z. Yuan, Y. Liu, Y. He and F. Y. Xie, *Mater. Sci. Eng., A*, 2003, **363**, 140–151.
15 D. Simonovic and M. H. F. Sluiter, *Phys. Rev. B: Condens. Matter Mater. Phys.*, 2009, **79**, 054304.
16 R. Abbaschian and R. E. Reed-Hill, *Physical Metallurgy Principles*, Cengage Learning, Stamford CT, Fourth edn, 2009.

17 D. N. Seidman, E. A. Marquis and D. C. Dunand, *Acta Mater.*, 2002, **50**, 4021–4035.
18 J. Gröbner, D. Mirković and R. Schmid-Fetzer, *Metall. Mater. Trans. A*, 2004, **35**, 3349–3362.
19 L. Jin, Y.-B. Kang, P. Chartrand and C. D. Fuerst, *CALPHAD*, 2011, **35**, 30–41; Y.-B. Kang, A. D. Pelton, P. Chartrand and C. D. Fuerst, *CALPHAD*, 2008, **32**, 413–422.
20 D. Huang, S. Liu, Y. Tang, Y. Du, P. Nash and B. Sundman, *Thermochim. Acta*, 2016, **646**, 49–58.
21 G. Rother, J. R. Keiser, M. P. Brady, K. A. Unocic, L. M. Anovitz, K. C. Littrell, R. A. Peascoe-Meisner, M. L. Santella, D. J. Wesolowski and D. R. Cole, *Corros. Sci.*, 2012, **58**, 121–132; M. J. Berg, *J. Quant. Spectrosc. Radiat. Transfer*, 2012, **113**, 2292–2309.
22 W. Wu, K. An, L. Huang, S. Y. Lee and P. K. Liaw, *Scr. Mater.*, 2013, **69**, 358–361.
23 B. Clausen and M. A. M. Bourke, *Metall. Mater. Trans. A*, 2001, **32**, 691–694.
24 H. Choo, B. S. Majumdar, P. Rangaswamy and M. A. M. Bourke, *Adv. X-Ray Anal.*, 2003, **46**, 245.
25 L. Xiaochun, Y. Yang and D. Weiss, *Metall. Sci. Technol.*, 2008, **26**, 12; S. C. Tjong and Z. Y. Ma, *Mater. Sci. Eng., R*, 2000, **29**, 49–113.
26 C. R. Brooks, *Heat Treatment, Structure and Properties of Nonferrous Alloys*, American Society for Metals, Metals Park OH, 1982.
27 K. Binnemans, P. T. Jones, K. Van Acker, B. Blanpain, B. Mishra and D. Apelian, *JOM*, 2013, **65**, 846–848.
28 N. Saunders and A. P. Miodownik, *CALPHAD: (Calculation of Phase Diagrams): A Comprehensive Guide*, Elsevier, New York, 1998.
29 J. Ilavsky, F. Zhang, A. J. Allen, L. E. Levine, P. R. Jemian and G. G. Long, *Metall. Mater. Trans. A*, 2013, **44**, 68–76.
30 F. Lixin, D. Mike, B. Scott, G. Nick and I. Jan, *J. Phys.: Conf. Ser.*, 2010, **247**, 012005.
31 K. An, H. D. Skorpenske, A. D. Stoica, D. Ma, X.-L. Wang and E. Cakmak, *Metall. Mater. Trans. A*, 2011, **42**, 95–99.
32 D. Yu, K. An, Y. Chen and X. Chen, *Scr. Mater.*, 2014, **89**, 45–48; D. Yu, H. Bei, Y. Chen, E. P. George and K. An, *Scr. Mater.*, 2014, **84–85**, 59–62.
33 Y. Chen, D. Yu and K. An, *Mater. Res. Lett.*, 2017, **5**, 89–94.

